

Non-uniform heat redistribution among multiple channels in the integer quantum Hall regime

Ryota Konuma,¹ Chaojing Lin,¹ Tokuro Hata,¹ Taichi Hirasawa,¹
Takafumi Akiho,² Koji Muraki,² and Toshimasa Fujisawa^{1,*}

¹*Department of Physics, Tokyo Institute of Technology,
2-12-1 Ookayama, Meguro, Tokyo, 152-8551, Japan.*

²*NTT Basic Research Laboratories, NTT Corporation,
3-1 Morinosato-Wakamiya, Atsugi 243-0198, Japan.*

(Dated: June 22, 2022)

Heat transport in multiple quantum-Hall edge channels at Landau-level filling factor $\nu = 2, 4,$ and 8 is investigated with a quantum point contact as a heat generator and a quantum dot as a local thermometer. Heat distribution among the channels remains highly non-uniform, which can be understood with the plasmon eigenmodes of the multiple channels. The heat transport can be controlled with another quantum point contact as a quantized heat valve, as manifested by stepwise increases of heat current at the thermometer. This encourages developing integrated heat circuits with quantum-Hall edge channels.

I. INTRODUCTION

Recent developments in quantum thermoelectric devices, such as heat engines and refrigerators based on quantum-dot (QD) and superconducting circuits, are attractive for manipulating heat in beneficial ways.^{1–10} Even though each device works efficiently, the ordinary heat diffusion process between these devices can degrade the overall thermal efficiency dramatically.^{9,10} This issue can be overcome by using chiral heat transport in quantum Hall (QH) edge channels. In the integer QH regime, heat travels unidirectionally in a certain direction determined by the direction of the magnetic field.^{11–15} Each channel has a quantized thermal conductance as well as a quantized electronic conductance.¹⁶ For typical edge channels in AlGaAs/GaAs heterostructures, the heat is mostly conserved in the channels within a dissipation length of about $30 \mu\text{m}$.^{17,18} These characteristics are attractive for designing an integrated heat circuit, where functional thermoelectric devices are efficiently connected by QH edge channels. Fundamental heat transport in nanostructures, such as thermal Coulomb blockade, has been successfully studied.^{19–21}

Besides the fundamental heat transport characteristics, QH edge channels have unique characteristics of a Tomonaga-Luttinger (TL) liquid as extensively studied at Landau-level filling factor $\nu = 2$.^{22–25} When one of the two channels is heated with a quantum point contact (QPC), the Coulomb interaction redistributes the charge and heat in the two channels.^{26–30} This heat redistribution occurs in a deterministic way in terms of spin-charge separation. Because this process can be understood as plasmon scattering at discontinuities, i.e., the charge injection points for the above cases, the electronic state may remain in a non-thermal metastable state during the transport in clean channels.^{17,31,32} This is not the case for a diffusion process with stochastic scattering events.³³ One can utilize such QH channels for transferring heat from one functional device to another efficiently

without maximizing the entropy of the carriers. While the two-channel configuration at $\nu = 2$ is the archetypal case for the TL model, one can also expect similar behavior for multiple channels at higher ν . Observation of non-uniform heat redistribution among the channels would justify the applicability of the TL physics.

In this work, we investigate heat transport through multiple QH edge channels from a QPC heat generator to a QD thermometer at $\nu = 2, 4,$ and 8 in an AlGaAs/GaAs heterostructure. When a particular channel is heated with the QPC, the heat is redistributed among the co-propagating channels in a non-uniform way independent of the propagation distance. This is consistent with the plasmon modes of the TL liquid with multiple channels. We also demonstrate that the heat transport can be controlled with another QPC as a heat valve placed in the edge channels, as manifested by stepwise increases of heat current at the QD thermometer. Our experiment encourages developing integrated heat circuits with QH edge channels in integrated heat circuits.

II. HEAT CIRCUIT

Figure 1(a) shows a schematic diagram of edge channels for studying heat transport at $\nu = 4$. Four chiral channels with index i ($= 1, 2, 3,$ and 4 from the outer to the inner one) are formed along the edges of the incompressible regions (light blue) under perpendicular magnetic field B . Heat can be introduced from the first QPC (QPC1) to the left segment of the target channels of length L_1 . This heat is redistributed in the four channels during the transport and partitioned at the second QPC (QPC2). The transmitted heat is redistributed again in the right segment of length L_2 , and the resulting electronic excitation is investigated by a QD spectrometer. With this setup, we demonstrate tunable heat transport through QPC2 as a heat valve. The operation principle of each device is described in the following before showing

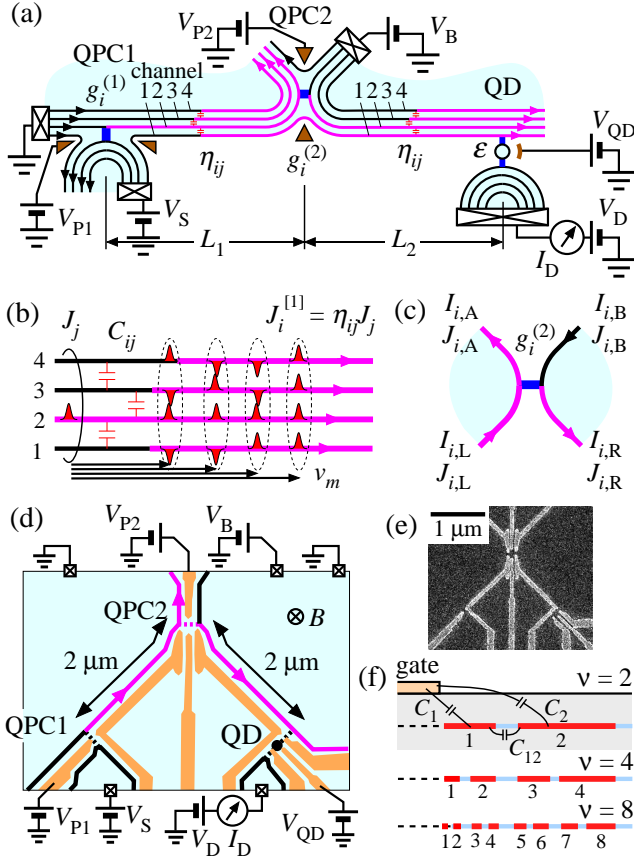


FIG. 1. (a) Schematic of the heat transport measurement with QPC1 as a heat generator, QPC2 as a heat valve, and QD as a heat detector. Four QH edge channels 1 - 4 with chirality depicted by the arrows are heated in the magenta regions. (b) Fractionalization process in the 4 channels when a charge pulse is introduced in channel 2. Plasmon modes with coupled wavepackets in ovals carry heat. (c) Partition process at a QPC for heat current $J_{i,p}$ and charge current $I_{i,p}$ in channel i at port $p \in \{L, R, A, B\}$. (d) Schematic device structure with a measurement setup. (e) Scanning electron micrograph of a control sample. (f) Schematic channel geometries at $\nu = 2, 4$, and 8 .

the experimental results.

By applying a source voltage V_S across QPC1, charge and heat currents can be introduced to channel i with transmission coefficient $g_i^{(1)}$. By assuming energy independent $g_i^{(1)}$ for simplicity, electrochemical potential $\mu_i = e g_i^{(1)} V_S$, charge current $I_i = \frac{e^2}{h} g_i^{(1)} V_S$, and heat current $J_i = \frac{1}{2h} g_i^{(1)} (1 - g_i^{(1)}) V_S^2$ are induced in the channels, where e is the elementary charge and h is the Planck constant.^{20,34} For example, Fig. 1(a) shows that the heat is introduced from QPC1 to channel 2 with $g_1^{(1)} = 1$, $g_2^{(1)} = 0.5$, and $g_3^{(1)} = g_4^{(1)} = 0$.

In the presence of inter-channel Coulomb interaction, the heat current is redistributed during the transport in the copropagating channels. The inter-channel tunneling

is weak in the following experiment and thus neglected for simplicity. The heat current in one-dimensional channels can be expressed as an ensemble of plasmons (charge density waves), which describe electronic excitation from the ground state.³¹ In the low-energy limit, the plasmons can be described as superpositions of the transport eigenmodes determined by the Coulomb interaction. This description was successful in studying heat transport and non-thermal states at $\nu = 2$.³⁵⁻³⁸ We apply this scheme to higher ν ($2 - 8$) in this work. Figure 1(b) illustrates how a single charge wave packet generated in $i = 2$ channel splits into four coupled wavepackets (enclosed by dashed ovals) propagating at different velocities v_m for eigenmode m . This is a kind of fractionalization in which an electron wave packet from a point contact is fractionalized into several quasiparticles. By considering the initial packet of time width $\Delta t = \hbar/eV_S$, the fractionalization should develop after traveling the fractionalization length $L_F = \max_{m \neq n} \left\{ \frac{v_m v_n}{|v_m - v_n|} \Delta t \right\}$, as derived in Appendix. Such electronic wave packets randomly injected from a QPC are redistributed in all channels, which is the microscopic picture of the heat redistribution. By introducing the heat fractionalization factor η_{ij} from channel j to channel i , the heat current in channel i after the fractionalization can be written as $J_i^{[1]} = \sum_j \eta_{ij} J_j$, where the superscript [1] denotes the first fractionalization process. The plasmon scattering model suggests reciprocal relation $\eta_{ij} = \eta_{ji}$, as shown in Appendix. This factor is determined by the strengths of inter-channel Coulomb interactions and should be different from equipartition ($\eta_{ij} = 1/N$ for N channels) expected in ordinary thermal conduction associated with the diffusive motion of electrons or phonons in materials.

The heat transport can be controlled by using QPC2 with transmission coefficient $g_i^{(2)}$ for channel i . Considering that the electronic states in the channels are correlated as depicted in Fig. 1(b), the TL characteristics such as the power-law anomaly in the conductance may appear in this tunneling process. Here, we shall ignore it for simplicity. This may be justified if $g_i^{(2)}$ is not very close to 0 and 1, where previous measurements with QD spectroscopy did not find the non-thermal states associated with the TL liquid.¹⁷ Therefore, we assume that each electron in the input channels is allowed to tunnel stochastically to the output channels. This partition process for i -th channel is schematically shown in Fig. 1(c) for two input (L and B) and two output (A and R) ports with finite $g_i^{(2)}$. One can show how heat currents $J_{i,L}$ and $J_{i,B}$ as well as charge currents $I_{i,L} = \frac{e}{h} \mu_{i,L}$ and $I_{i,B} = \frac{e}{h} \mu_{i,B}$ with chemical potentials $\mu_{i,L}$ and $\mu_{i,B}$ will be partitioned with $g_i^{(2)}$ for arbitrary single-particle distribution functions. The output charge current $I_{i,R}$ and heat current $J_{i,R}$ are given by

$$I_{i,R} = g_i^{(2)} I_{i,L} + (1 - g_i^{(2)}) I_{i,B} \quad (1)$$

$$J_{i,R} = g_i^{(2)} J_{i,L} + \left(1 - g_i^{(2)}\right) J_{i,B} \quad (2)$$

$$+ \frac{1}{2h} g_i^{(2)} \left(1 - g_i^{(2)}\right) (\mu_{i,L} - \mu_{i,B})^2$$

where energy independent $g_i^{(2)}$ is assumed for simplicity. Equation (2) shows that the heat partition at QPC2, described in the first and second terms, can be controlled with $g_i^{(2)}$, while the heat generation at the QPC2, given by the third term, can be zeroed by setting $\mu_{i,L} = \mu_{i,B}$. The latter is particularly useful to discriminate the heat partition from heat generation at QPC2.

The heat partitioned at QPC2 is redistributed in the right segment of the target channels with the same η_{ij} as the left one. The resulting heat current in channel i after the second partition should be given by $J_i^{[2]} = \sum_j \eta_{ij} J_{j,R}$ from the above assumptions. We can experimentally investigate $J_1^{[2]}$ in the outermost channel by using a QD energy spectrometer.³⁹ For a single energy level ε in the QD weakly coupled to the channel, the current $I_D = e\Gamma [f_1(\varepsilon) - f_D(\varepsilon)]$ with the single-electron tunneling rate Γ measures the tunneling distribution function $f_1(\varepsilon)$ of interest if the distribution function $f_D(\varepsilon)$ of the drain electrode is known. The chemical potential $\mu_1 = \int_{-\infty}^{\infty} [f_1(E) - f_{FD}(E; \mu = 0, T = 0)] dE$ and heat current $J_1 = \frac{1}{h} \int_{-\infty}^{\infty} E [f_1(E) - f_{FD}(E; \mu_1, T = 0)] dE$ can be obtained from $f_1(\varepsilon)$, where $f_{FD}(E; \mu, T)$ is the Fermi distribution function at chemical potential μ and temperature T . If $f_1(\varepsilon)$ is approximated with $f_{FD}(E; \mu_1, T_1)$, the corresponding heat current $J_1 = \frac{\pi^2}{6h} k_B^2 T_1^2$ can be estimated from the effective temperature T_1 of the channel.

While energy-independent g_i is assumed in the above analysis, the transmission coefficient can be energy-dependent in an actual device. In this case, g_i can be understood as the average coefficient for the energy range of interest for μ_i and I_i . Importantly, the energy-dependent tunneling induces thermoelectric effects, which modify Eqs. (1) and (2). For example, different input temperatures with $J_{i,L} \neq J_{i,B}$ causes thermoelectric potential ($\mu_{i,R} \neq \mu_{i,A}$) in the outputs even when no potential bias is given in the inputs ($\mu_{i,L} = \mu_{i,B}$). Even in the absence of input heat currents ($J_{i,L} = J_{i,B} = 0$), the heat generation of the third term of Eq. (2) is modified to cause asymmetric heat currents in the outputs ($J_{i,R} \neq J_{i,A}$). Such non-linear effects will be discussed later with the experiment.

III. EXPERIMENTAL RESULTS

A. Device

The above heat transport was investigated with a device fabricated in a standard AlGaAs/GaAs heterostructure with an electron density of $1.85 \times 10^{11} \text{ cm}^{-2}$ and electron mobility on the order of $10^6 \text{ cm}^2/\text{Vs}$ at low temperature. A schematic device structure and a scanning electron micrograph of a control device are shown in Figs.

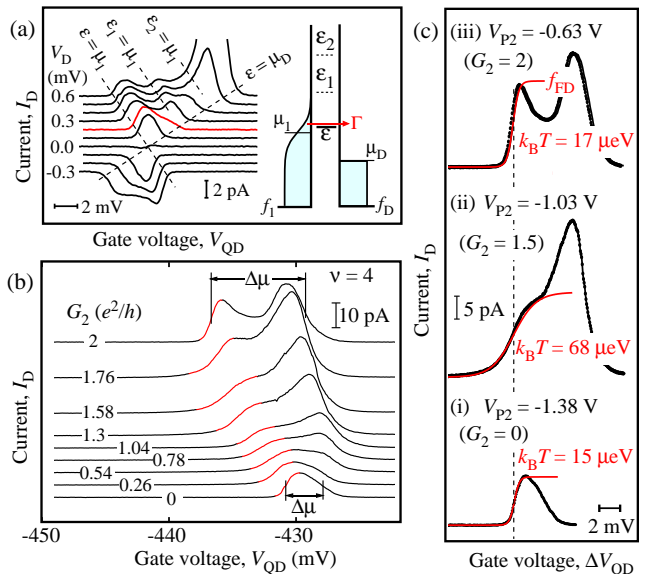


FIG. 2. (a) Single-electron transport characteristics of the QD at $B = 1.8 \text{ T}$ ($\nu = 4$). The inset shows the energy diagram with the dot levels, ε , ε_1 , and ε_2 . The QD spectroscopy was performed with small bias typically at $V_D = 0.2 \text{ mV}$ (the red trace). (b) QD current spectrum at $V_D = 0.2 \text{ mV}$ obtained when the current and heat were introduced from QPC2 at $V_S = -0.3 \text{ mV}$ with several conductance G_2 values. The current onset in red is broadened at $G_2 \sim 0.5$ and 1.5 . The width of the conductive region measures $\Delta\mu$. (c) The current profiles (black lines) fitted with the Fermi distribution function (red lines) around the onset.

1(d) and 1(e), respectively. Under perpendicular magnetic field, $B = 3.3 \text{ T}$ ($\nu \simeq 2$), 1.8 T ($\nu \simeq 4$), and 0.9 T ($\nu \simeq 8$), QPC1, QPC2, and QD were formed by applying appropriate voltages on the gates. We restricted ourselves to these even filling factors to ensure a large energy gap in the bulk. All measurements were performed at a base temperature of about 30 mK , and the QD thermometry shows an effective electron temperature of about 170 mK in the absence of QPC heating (due to external noise in the experimental environment).

Figure 2(a) shows the Coulomb blockade characteristics of the QD obtained at $B = 1.8 \text{ T}$ ($\nu \simeq 4$), where both QPCs were fully open for reference and the QD was biased by varying V_D at $V_S = 0$. The current I_D increases stepwise when energy levels ε of the ground state and ε_1 and ε_2 of the first and second excited states enter the transport window between the chemical potentials $\mu_1 (= 0)$ and $\mu_D = eV_D$. The stepwise feature is pronounced with a peak associated with the Fermi-edge singularity.⁴⁰ This many-body effect is smeared out when the heat is introduced to the channel and thus neglected in the following analysis. For all the spectroscopy measurements presented below, we apply small but finite energy bias $\Delta\mu = \mu_1 - \mu_D = 0.1 - 0.5 \text{ meV}$ to allow us to investigate the distribution function $f_1(E)$ at around $\varepsilon \sim \mu_1$.

B. Heat redistribution

First, we investigate heat redistribution among copropagating edge channels, which is required for analyzing the heat-valve characteristics. To confirm that the heat redistribution is independent of the propagating length, we compare two experiments with short ($L_2 = 2 \mu\text{m}$) and long ($L_1 + L_2 = 4 \mu\text{m}$) distances from QPC2 and QPC1, respectively, to the QD. For the short configuration, the charge and heat were introduced from QPC2 at various conductance $G_2 = \sum_i g_i^{(2)}$, with $V_S = -0.3 \text{ mV}$ and QPC1 fully opened. QD current profiles were obtained with $V_D = 0.2 \text{ mV}$, as shown in Fig. 2(b). The width of the conductive region increases with G_2 , from which $\Delta\mu = \mu_1 - \mu_D$ can be estimated. The onset of the current step at around $\varepsilon \sim \mu_1$, which is highlighted in red, is broadened when the heat is injected to channel 1 at $G_2 \sim 0.5$ and channel 2 at $G_2 \sim 1.5$. The latter demonstrates the heat transfer from channel 2 to channel 1, meaning that the heat is redistributed between channels 1 and 2. The current profile around the onset can be fitted with the Fermi distribution function, as shown in Fig. 2(c). The effective temperature of $k_B T = 68 \mu\text{eV}$ estimated for $G_2 \sim 1.5$ is significantly greater than $k_B T = 15 - 17 \mu\text{eV}$ for $G_2 = 2$ and 0 that corresponds to the base temperature. Corresponding heat current $J = \frac{\pi^2}{6h} k_B^2 T^2$ ($\simeq 0.29 \text{ pW}$ at $G_2 \sim 1.5$) in channel 1 is obtained from the quantized heat conductance.

Figure 3(a) summarizes the gate voltage V_{P2} dependence of the QPC2 conductance G_2 in the top panel, $\Delta\mu = \mu_1 - \mu_D$ estimated from the width of the current peak in the middle panel, and the heat current J in the bottom panel. The tunneling regions with non-integer G are highlighted by four orange stripes. $\Delta\mu$ increases stepwise only in the leftmost stripe for the tunneling into channel 1. μ_1 increases to eV_S as soon as G_2 reaches 1, and stays almost constant ($\mu_1 \simeq eV_S$) even when the chemical potential of the second channel, μ_2 , is changed in the range of $0 < \mu_2 < eV_S$ ($1 < G_2 < 2$). This indicates that inter-channel tunneling is negligible. However, the heat behaves differently from the charge. The heat current J in channel 1 is enhanced in multiple tunneling regions, and the maximum J values are different for different tunneling regions. As the heat is originally generated in one of the four channels at the QPC, the heat is redistributed non-uniformly among the channels during the transport before reaching the QD spectrometer. By assuming that identical heat $J_j = \frac{1}{8h} (eV_S)^2$ ($= 0.43 \text{ pW}$ for $eV_S = 0.3 \text{ meV}$) is generated in the j -th channel at $g_j^{(2)} = 0.5$ in the j -th stripe, the maximum heat current $J = \eta_{1j} J_j$ measures the heat partition factor η_{1j} ; $\eta_{11} \simeq \eta_{12} \simeq 0.5$, $\eta_{13} \simeq 0.06$, and $\eta_{14} \simeq 0$ for the data in Fig. 3(a) with propagation length $L_2 = 2 \mu\text{m}$. This indicates efficient heat transfer between channels 1 and 2, while heat transfer from channels 3 and 4 is inefficient. Since the sum is close to unity ($\sum_i \eta_{i1} = \sum_j \eta_{1j} \simeq 1$), the heat is well conserved within the multiple channels.

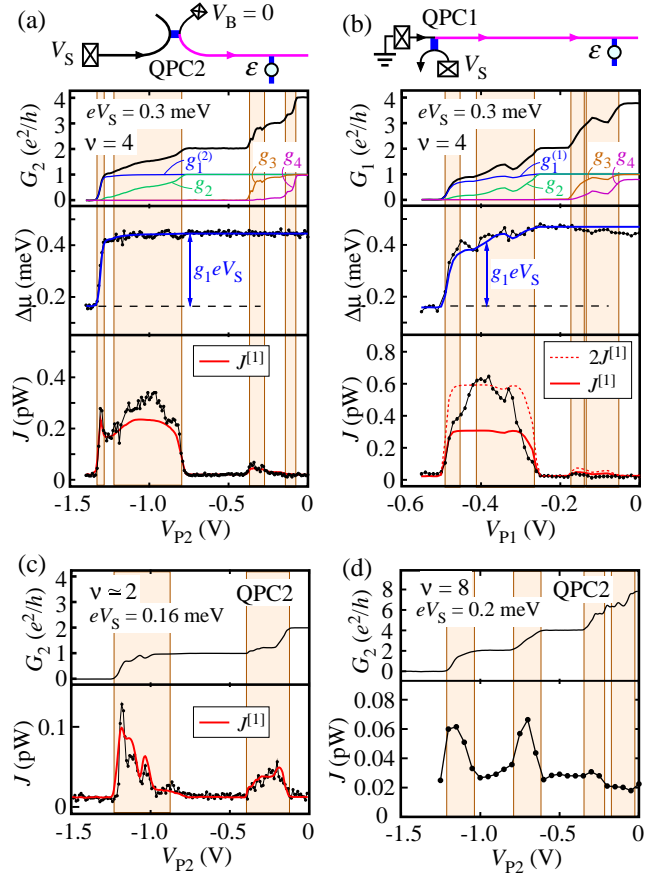


FIG. 3. Summary of single QPC experiments showing conductance G_1 or G_2 in the top panels, $\Delta\mu = \mu_1 - \mu_D$ in the middle panels, and the heat current J in the bottom panels. (a) excited from QPC2 at distance $L_2 = 2 \mu\text{m}$ and $\nu = 4$, (b) excited from QPC1 at distance $L_1 + L_2 = 4 \mu\text{m}$ and $\nu = 4$, (c) excited from QPC2 at $\nu \simeq 2$, and (d) excited from QPC2 at $\nu = 8$. The tunneling regions at non-integer G are highlighted with orange stripes. Schematic channel geometries with QPC1 and QPC2 are shown in the insets to (a) and (b).

The same experiment was performed for the long distance by varying the conductance G_1 of QPC1, while QPC2 was fully opened ($G_2 = 4$), as shown in Fig. 3(b). The conductance plateaus in G_1 are less clear as compared to those for QPC2, and similarly, the stepwise increase of $\Delta\mu$ in the middle panel is not as sharp as that for QPC2. As a result, the heat current J in the bottom panel shows a broad peak spread over the leftmost and second-left tunneling regions. It should be noted that the heat currents in the third and fourth tunneling regions remain low, comparable to those for QPC2. This implies that a fixed fraction of the heat generated in the respective channels comes to channel 1 in agreement with the plasmon transport model. If the heat redistribution was mediated by a diffusion process, the heat should be redistributed more uniformly for longer propagation lengths.

Moreover, similar heat redistributions (η_{1j}) at 2 and 4 μm suggest that the fractionalization length L_F is shorter than 2 μm in agreement with the previous study ($L_F \simeq 0.3 \mu\text{m}$ at $V_S = 0.3 \text{ mV}$ for $\nu = 2$).¹⁷

We next compare the fractionalization at different filling factors, $\nu \simeq 2$ ($B = 3.3 \text{ T}$) [Fig. 3(c)] and $\nu = 8$ [Fig. 3(d)], with that at $\nu = 4$ [Fig. 3(a)], for injection from QPC2. Strongly non-uniform heat distribution is seen in all cases; $\eta_{11} \simeq 0.7$ and $\eta_{12} \simeq 0.3$ at $\nu = 2$ and $\eta_{11} + \eta_{12} \simeq \eta_{13} + \eta_{14} \simeq 0.5$, $\eta_{15} + \eta_{16} \simeq 0.05$, and $\eta_{17} + \eta_{18} \simeq 0$ at $\nu = 8$. This might be reasonable by considering that the locations of edge channels at different ν are related to each other, as schematically shown in Fig. 1(f). Namely, if large non-uniformity with $\eta_{11} > \eta_{12}$ is seen at $\nu = 2$, similar or even larger non-uniformity with $\eta_{11}, \eta_{12} > \eta_{13}, \eta_{14}$ should appear at $\nu = 4$ by considering that the channels 2 and 3 are greatly separated by the cyclotron energy. Such non-uniformity can be related to the asymmetric channel structure with different channel capacitances $C_1 \neq C_2$ for $\nu = 2$. Similar asymmetry was seen in previous charge-fractionalization experiments; for example $\eta_{11} \simeq 0.55$ and $\eta_{12} \simeq 0.45$ at $\nu = 2$ (see Appendix).³⁰

To justify the above analysis, the expected heat current $J_i^{[1]}$ is calculated in the following way. Because the plateaus at $G = 1$ and 3 are not well quantized, insufficient spin splitting is considered to decompose G_1 and G_2 to $g_i^{(1)}$ and $g_i^{(2)}$, respectively, as shown by the colored lines in Fig. 3(a) and (b). The inter-channel tunneling is neglected for simplicity. To this end, we use a saddle point potential to characterize a QPC, which allows us to relate g_1 and g_2 through a single parameter α as $g_2^{-1} - 1 = \alpha (g_1^{-1} - 1)$. Here, $\alpha = 2\pi\Delta/\hbar\omega_x$ is determined by the energy gap (spin splitting) Δ and the characteristic energy $\hbar\omega_x$ of the barrier potential.^{41,42} The parameter α is determined from the deviation of $\Delta\mu$ from eV_S at $G = 1$ ($\alpha \simeq 16$ for QPC1 showing $g_1^{(1)} \simeq 0.8$ and $g_2^{(1)} \simeq 0.2$ at $G_1 = 1$, and $\alpha \simeq 100$ for QPC2 showing $g_1^{(2)} \simeq 0.9$ and $g_2^{(2)} \simeq 0.1$ at $G_2 = 1$). This α was used to decompose $G = g_1 + g_2$ into g_1 and g_2 for the data at $G \leq 2$, by assuming constant α . As the $G = 2$ plateau is clear, g_3 and g_4 should be zero at $G \leq 2$, and g_1 and g_2 should be 1 at $G \geq 2$. For the data at $2 \leq G \leq 4$, the same α was used to decompose $G = 2 + g_3 + g_4$ into g_3 and g_4 , as shown in the figures. The obtained g_i explains the variation of $\Delta\mu$ as shown by the blue line $g_i eV_S$ in the middle panels of Figs. 3(a) and (b). The heat current $J^{[1]}$ is calculated from the above g_i and $\eta_{11} = \eta_{12} = 0.47$, $\eta_{13} = 0.06$, and $\eta_{14} = 0$, as shown by the red line in the bottom panels in Figs. 3(a) and 3(b). A similar analysis was made for the data in Fig. 3(c), where the decomposition of $G = g_1 + g_2$ is well defined with a large spin splitting at higher B . The obtained $J^{[1]}$ with $\eta_{11} \simeq 0.7$ and $\eta_{12} \simeq 0.3$ reproduces the data. The analysis was not made for the data in Fig. 3(d) as the spin splitting is not resolved at $\nu = 8$. Consistency with the above $J^{[1]}$ values at $\nu = 2$ and 4 for QPC2 supports the non-uniform heat

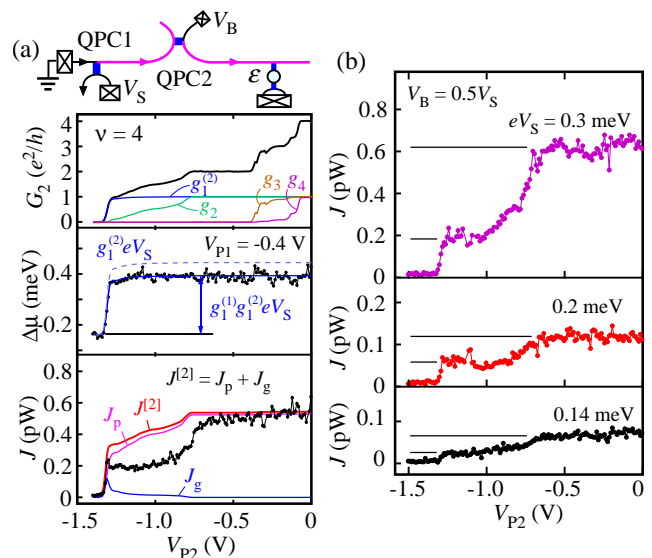


FIG. 4. Summary of double QPC experiments. (a) G_2 in the top panel [same as in Fig. 3(a)], $\Delta\mu$ in the middle panel, and the heat current J in the bottom panel. The data was obtained at $V_B = 0$ and $B = 1.8 \text{ T}$ ($\nu \simeq 4$). The upper inset shows a schematic channel configuration. (b) Heat current J obtained at several eV_S , where $V_B = V_S/2$ was chosen to reduce the heat generation J_g at QPC2.

redistribution under heat conservation.

Here we comment on the large deviation of the observed J from the estimated $J^{[1]}$ in Fig. 3(b) with QPC1 showing imperfect quantized conductance. Our analysis assumes that the heat generated at QPC1 is equally split between the left- and right-going downstream channels. However, in the presence of nonlinearity in the QPC1, this is no longer true. Generally, electrons at higher energies are likely to have higher transmission coefficients through the QPC barrier. Therefore, the heat current can be increased up to $2J^{[1]}$ [the dashed line in the bottom panel of Fig. 3(b)] with the $J^{[1]}$ estimated from the above procedure.

C. Heat valve

We demonstrate tunable heat transport through QPC2 as a heat valve. As shown in Fig. 1(a) and the inset to Fig. 4(a), the two QPCs as well as the QD spectrometer were activated. Heat is generated with QPC1 at $V_{P1} = -0.4 \text{ V}$ ($g_1^{(1)} \simeq 0.8$, $g_2^{(1)} \simeq 0.3$, and $g_3^{(1)} \simeq g_4^{(1)} \simeq 0$) and $\nu = 4$, and should be redistributed mostly in channels 1 and 2 before reaching QPC2. This heat is partially transferred to the right segment through QPC2 and redistributed again in the channels before reaching the QD detector. The heat current in the right segment should be controlled by the conductance of QPC2 acting as a heat valve.

Figure 4(a) summarizes $\Delta\mu$ in the middle panel and J

in the bottom panel extracted from the QD spectroscopy, as well as G_2 in the top panel. The measured $\Delta\mu$ (dots) follows $g_1^{(1)}g_1^{(2)}eV_S$ (the solid line) with $g_1^{(1)} = 0.8$ and $g_1^{(2)}$ shown in the top panel. This indicates that the two QPCs are working well in agreement with the characteristics obtained separately. The heat current J shows a double-step structure associated with the heat partition between channels 1 and 2. This demonstrates the heat-valve action with QPC2. In this experiment, the step heights in J should depend on the heat fractionalization ratio η_{ij} . The first and second steps associated with channels 1 and 2 have similar step heights, as $\eta_{11} \simeq \eta_{12}$ in our device. The device should also control the heat transport in channels 3 and 4, whereas corresponding step structures are not visible due to the small η_{13} and η_{14} of our device.

The expected heat current $J^{[2]}$ based on Eq. (2) and η_{ij} is plotted as a thick line together with the heat partition J_p [the first and the second terms of Eq. (2)] and heat generation J_g (the third term) in the bottom panel of Fig. 4(a). This suggests that the heat partition should be responsible for the overall double-step structure in J . However, quantitative difference between the calculated $J^{[2]}$ and measured J is seen. The observed stepwise feature of J is much sharper than that of $J^{[2]}$ calculated from G_2 , with the much wider first plateau. While we do not have reasonable explanation for this, the difference might involve the ignored many-body effect of the fractionalized quasiparticles.

The calculation suggests that the heat generation is significant only in the first step where a finite bias $\mu_1 = g_1^{(1)}eV_S \simeq 0.24$ meV is applied across QPC2 in channel 1 for $V_B = 0$. One can reduce the heat generation in channel 1 by adjusting eV_B at μ_1 , while this induces heat generation in other channels (finite eV_B against $\mu_i = 0$ for $i \geq 2$). Considering that the heat current is proportional to the square of the bias, a compromising choice is choosing $V_B = V_S/2$. We also confirmed the step-like control of J for several V_S values with $V_B = V_S/2$, as shown in Fig. 4(b).

Unfortunately, the nonlinearity of the QPC conductance hinders further quantitative analysis. For example, the QPC conductances G_1 and G_2 change slightly with the applied bias (not shown). The heat current even without forming QPC2 at $V_{P2} = 0$ in Fig. 4(b) increases with V_S more rapidly as compared to the expected V_S^2 dependence. Such non-linearity may change α and η_{ij} , and cause some thermoelectric effects. This could be the reason why the ratio of the first and second step heights in J changes with V_S . Such non-linear effects as well as the many-body effects should be considered to understand the observed behaviors.

IV. SUMMARY

In summary, heat transport through multiple QH edge channels is investigated with a QPC heat injector, a QPC heat valve, and a QD thermometer in the QH regime at $\nu = 2, 4$, and 8 in an AlGaAs/GaAs heterostructure. The heat fractionalization in the interacting channels is consistent with plasmon transport model. The heat valve action is qualitatively consistent with the single-particle tunneling at the QPC, while quantitative difference may involve many-body effects and non-linear effects. The results encourage us to study integrated heat circuits with QH edge channels.

ACKNOWLEDGMENTS

We thank Shunya Akiyama for experimental supports. This work was supported by JSPS KAKENHI JP19H05603 and Nanotechnology Platform Program at Tokyo Institute of Technology.

Appendix A: Heat redistribution

The electronic heat is particle-hole excitations around the Fermi energy and propagates in a form of charge density waves (plasmons) in the low energy limit. We employ the distributed capacitance model to describe charge density waves in multiple edge channels, as shown in Fig. 1(b). The charge density $\rho = \{\rho_i(x, t)\}$, the potential $\mathbf{V} = \{V_i(x, t)\}$, and time-dependent current $\mathbf{I} = \{I_i(x, t)\}$ in vector representations for channel i are defined as a function of coordinate x along the channels and time t . The electrostatic effects on the occupation of the channels can be written in a simple form of $\rho = \mathbf{C}\mathbf{V}$ with the capacitance matrix $\mathbf{C} = \{C_{ij}\}$ including self capacitance C_i and inter-channel capacitance C_{ij} . The quantized conductance $\sigma_q = \frac{e^2}{h}$ relates $\mathbf{I} = \sigma_q\mathbf{V}$. By using the current conservation rule ($\frac{\partial}{\partial t}\rho = -\frac{\partial}{\partial x}\mathbf{I}$), one can extract the unidirectional wave equation of the form $\frac{\partial}{\partial t}\mathbf{I} = -\sigma_q\mathbf{C}^{-1}\frac{\partial}{\partial x}\mathbf{I}$. Arbitrary waves can be written with orthonormal eigenmode $\tilde{\mathbf{I}}_m = \{\tilde{I}_{mi}\}$ and the velocity v_m for mode index m , where $\tilde{\mathbf{I}}_m \cdot \tilde{\mathbf{I}}_n = \delta_{mn}$. Detailed derivation and relation to the field theory are described in Refs.^{25,31}. This scheme was successful in studying charge dynamics in integer and fractional QH channels.^{30,43,44}

When a current fluctuation $I_n(x=0, t)$ is introduced, from a QPC in the present case, at $x=0$ only in channel n , current fluctuation at $x > 0$ in channel m is given by

$$I_m(x, t) = \sum_k \tilde{I}_{km}\tilde{I}_{kn}I_n\left(0, t - \frac{x}{v_k}\right).$$

The heat current $J_m(x) = \frac{1}{2}\sigma_q^{-1}\langle(\Delta I_m(x, t))^2\rangle$ can be calculated from the fluctuating part $\Delta I_m(x, t) =$

$I_m(x, t) - \langle I_m \rangle$ from the average $\langle I_m \rangle$, and is given by

$$J_m(x) = \frac{1}{2} \sigma_q^{-1} \sum_{k,l} \tilde{I}_{km} \tilde{I}_{kn} \tilde{I}_{lm} \tilde{I}_{ln} \phi \left(\frac{x}{v_l} - \frac{x}{v_k} \right),$$

where $\phi(\Delta t) = \langle \Delta I_n(0, t) \Delta I_n(0, t - \Delta t) \rangle$ is the correlation function of the input current fluctuation. We assume Lorentzian spectrum with $\phi(\Delta t) = a \exp(-t/\tau)$, where $a = \langle (\Delta I_n(0, t))^2 \rangle$ is the mean square of the input fluctuation and $\tau = \frac{\hbar}{eV_S}$ is the correlation time. Then, the heat current reaches the steady state at $x \gg L_F$, where the fractionalization length L_F is defined as $L_F = \max_{m \neq n} \left\{ \frac{v_m v_n}{|v_m - v_n|} \Delta t \right\}$. Therefore, the steady heat current $J_m(\infty)$ at $x \rightarrow \infty$ can be written as

$$\begin{aligned} J_m(\infty) &= \frac{1}{2} a \sigma_q^{-1} \sum_k \left(\tilde{I}_{km} \tilde{I}_{kn} \right)^2 \\ &= \eta_{mn} J_n(0), \end{aligned}$$

where $J_n(0) = \frac{1}{2} a \sigma_q^{-1}$ is the initial heat current, and

$\eta_{mn} = \sum_k \left(\tilde{I}_{km} \tilde{I}_{kn} \right)^2$ is the heat fractionalization factor discussed in this paper. This form suggests reciprocal relation $\eta_{mn} = \eta_{nm}$ in the heat redistribution.

For example, a system with two copropagating integer channels at $\nu = 2$ can be written with eigenmodes

$$\tilde{\mathbf{I}}_1 = \begin{pmatrix} \cos \theta \\ \sin \theta \end{pmatrix} \text{ and } \tilde{\mathbf{I}}_2 = \begin{pmatrix} \sin \theta \\ -\cos \theta \end{pmatrix}$$

by using mixing angle θ ($0 \leq \theta \leq \pi/4$). Corresponding heat fractionalization ratio reads

$$\begin{aligned} \eta_{11} &= \eta_{22} = \cos^4 \theta + \sin^4 \theta \\ \eta_{21} &= \eta_{12} = 1 - \eta_{11}. \end{aligned}$$

This allows us to calculate η_{ij} from the charge fractionalization data in previous reports ($\eta_{11} = 0.55$ for $\theta = 0.2\pi$ at $\nu = 2$).³⁰ Since the eigenmode $\tilde{\mathbf{I}}_m$ is determined by the capacitance matrix \mathbf{C} of the device, η_{mn} should depend on the sample and may be controlled by tailoring the electrostatic geometry.

-
- * fujisawa@phys.titech.ac.jp
- ¹ J. Gemmer, M. Michel, and G. Mahler, *Quantum Thermodynamics*, Lecture Notes in Physics 784, (Springer, Berlin Heidelberg, 2009).
 - ² H. Thierschmann, R. Sánchez, B. Sothmann, F. Arnold, C. Heyn, W. Hansen, H. Buhmann and L. W. Molenkamp, Three-terminal energy harvester with coupled quantum dots, *Nat. Nanotechnol.* **10**, 854-858 (2015).
 - ³ J. V. Koski, A. Kutvonen, I. M. Khaymovich, T. AlaNissila and J. P. Pekola, On-Chip Maxwell's Demon as an Information-Powered Refrigerator, *Phys. Rev. Lett.* **115**, 260602 (2015).
 - ⁴ K. Y. Tan, M. Partanen, R. E. Lake, J. Govenius, S. Masuda and M. Möttönen, Quantum-circuit refrigerator, *Nat. Commun.* **8**, 15189 (2017).
 - ⁵ D. von Lindenfels, O. Gräß, C. T. Schmiegelow, V. Kaushal, J. Schulz, M. T. Mitchison, J. Gould, F. Schmidt-Kaler and U. G. Poschinger, Spin Heat Engine Coupled to a Harmonic-Oscillator Flywheel, *Phys. Rev. Lett.* **123**, 080602 (2019).
 - ⁶ G. Jaliel, R. K. Puddy, R. Sánchez, A. N. Jordan, B. Sothmann, I. Farrer, J. P. Griffiths, D. A. Ritchie and C. G. Smith, Experimental Realization of a Quantum Dot Energy Harvester, *Phys. Rev. Lett.* **123**, 117701 (2019).
 - ⁷ K. Ono, S. N. Shevchenko, T. Mori, S. Moriyama and F. Nori, Analog of a Quantum Heat Engine Using a Single-Spin Qubit, *Phys. Rev. Lett.* **125**, 166802 (2020).
 - ⁸ B. Dutta, D. Majidi, N. W. Talarico, N. Lo Gullo, H. Courtois and C. B. Winkelmann, Single-Quantum-Dot Heat Valve, *Phys. Rev. Lett.* **125**, 237701 (2020).
 - ⁹ M. Josefsson, A. Svilans, A. M. Burke, E. A. Hoffmann, S. Fahlvik, C. Thelander, M. Leijnse and H. Linke, A quantum-dot heat engine operating close to the thermodynamic efficiency limits, *Nat. Nanotechnol.* **13**, 920-924 (2018).
 - ¹⁰ A. Harzheim, J. K. Sowa, J. L. Swett, G. A. D. Briggs, J. A. Mol and P. Gehring, Role of metallic leads and electronic degeneracies in thermoelectric power generation in quantum dots, *Phys. Rev. Research* **2**, 013140 (2020).
 - ¹¹ R. Sánchez, B. Sothmann and A. N. Jordan, Chiral Thermoelectrics with Quantum Hall Edge States, *Phys. Rev. Lett.* **114**, 146801 (2015).
 - ¹² P. Samuelsson, S. Kheradsoud and B. Sothmann, Optimal Quantum Interference Thermoelectric Heat Engine with Edge States, *Phys. Rev. Lett.* **118**, 256801 (2017).
 - ¹³ R. Sánchez, J. Splettstoesser and R. S. Whitney, Nonequilibrium System as a Demon, *Phys. Rev. Lett.* **123**, 216801 (2019).
 - ¹⁴ F. Hajiloo, R. Sánchez, R. S. Whitney and J. Splettstoesser, Quantifying nonequilibrium thermodynamic operations in a multiterminal mesoscopic system, *Phys. Rev. B* **102**, 155405 (2020).
 - ¹⁵ A. Borin and E. Sukhorukov, Threshold effects in one-dimensional strongly interacting nonequilibrium systems, *Phys. Rev. B* **99**, 085430 (2019).
 - ¹⁶ S. Jezouin, F. D. Parmentier, A. Anthore, U. Gennser, A. Cavanna, Y. Jin and F. Pierre, Quantum Limit of Heat Flow Across a Single Electronic Channel, *Science* **342**, 601 (2013).
 - ¹⁷ K. Itoh, R. Nakazawa, T. Ota, M. Hashisaka, K. Muraki and T. Fujisawa, Signatures of a Nonthermal Metastable State in Copropagating Quantum Hall Edge Channels, *Phys. Rev. Lett.* **120**, 197701 (2018).
 - ¹⁸ H. le Sueur, C. Altimiras, U. Gennser, A. Cavanna, D. Maily, and F. Pierre, Energy Relaxation in the Integer Quantum Hall Regime, *Phys. Rev. Lett.* **105**, 056803 (2010).
 - ¹⁹ E. Sivre, A. Anthore, F. D. Parmentier, A. Cavanna, U. Gennser, A. Ouerghi, Y. Jin, and F. Pierre, Heat Coulomb blockade of one ballistic channel, *Nat. Phys.* **14**, 145 (2017).
 - ²⁰ E. Sivre, H. Duprez, A. Anthore, A. Aassime, F. D. Par-

- mentier, A. Cavanna, A. Ouerghi, U. Gennser and F. Pierre, Electronic heat flow and thermal shot noise in quantum circuits, *Nat. Commun.* **10**, 5638 (2019).
- ²¹ H. Duprez, F. Pierre, E. Sivre, A. Aassime, F. D. Parmentier, A. Cavanna, A. Ouerghi, U. Gennser, I. Safi, C. Mora and A. Anthore, Dynamical Coulomb blockade under a temperature bias, *Phys. Rev. Research* **3**, 023122 (2021).
- ²² T. Giamarchi, *Quantum Physics in One Dimension* (Oxford Univ. Press, 2004).
- ²³ I. Levkivskiy, *Mesoscopic Quantum Hall Effect* (Springer Theses), Springer-Verlag (2012).
- ²⁴ M. Hashisaka and T. Fujisawa, Tomonaga–Luttinger-liquid nature of edge excitations in integer quantum Hall edge channels, *Reviews in Physics* **3**, 32 (2018).
- ²⁵ T. Fujisawa, Nonequilibrium Charge Dynamics of Tomonaga–Luttinger Liquids in Quantum Hall Edge Channels, *Ann. Phys. (Berlin)* **2022**, 2100354 (2022).
- ²⁶ E. Berg, Y. Oreg, E.-A. Kim, and F. von Oppen, Fractional Charges on an Integer Quantum Hall Edge, *Phys. Rev. Lett.* **102**, 236402 (2009).
- ²⁷ V. Freulon, A. Marguerite, J. M. Berroir, B. Plaçais, A. Cavanna, Y. Jin and G. Féve, Hong-Ou-Mandel experiment for temporal investigation of single-electron fractionalization, *Nat. Commun.* **6**, 6854 (2015).
- ²⁸ E. Bocquillon, V. Freulon, J.-M Berroir, P. Degiovanni, B. Plaçais, A. Cavanna, Y. Jin and G. Féve, Separation of neutral and charge modes in one-dimensional chiral edge channels, *Nat. Commun.* **4**, 1839 (2013).
- ²⁹ H. Inoue, A. Grivnin, N. Ofek, I. Neder, M. Heiblum, V. Umansky, and D. Mahalu, Charge fractionalization in the integer quantum Hall effect, *Phys. Rev. Lett.* **112**, 166801 (2014).
- ³⁰ M. Hashisaka, N. Hiyama, T. Akiho, K. Muraki, and T. Fujisawa, Waveform measurement of charge- and spin-density wavepackets in a chiral Tomonaga–Luttinger liquid, *Nat. Phys.* **13**, 559 (2017).
- ³¹ K. Washio, R. Nakazawa, M. Hashisaka, K. Muraki, Y. Tokura, and T. Fujisawa, Long-lived binary tunneling spectrum in the quantum Hall Tomonaga-Luttinger liquid, *Phys. Rev. B* **93**, 075304 (2016).
- ³² I. P. Levkivskiy and E. V. Sukhorukov, Energy relaxation at quantum Hall edge, *Phys. Rev. B* **85**, 075309 (2012).
- ³³ H. Pothier, S. Guéron, N. O. Birge, D. Esteve and M. H. Devoret, Energy Distribution Function of Quasiparticles in Mesoscopic Wires, *Phys. Rev. Lett.* **79**, 3490 (1997).
- ³⁴ T. T. Heikkila, *The Physics of Nanoelectronics: Transport and Fluctuation Phenomena at Low Temperatures*, Oxford Univ. Pr. (2013).
- ³⁵ M. Hashisaka, K. Washio, H. Kamata, K. Muraki, and T. Fujisawa, Distributed electrochemical capacitance evidenced in high-frequency admittance measurements on a quantum Hall device, *Phys. Rev. B* **85**, 155424 (2012).
- ³⁶ M. Hashisaka, H. Kamata, N. Kumada, K. Washio, R. Murata, K. Muraki and T. Fujisawa, Distributed-element circuit model of edge magnetoplasmon transport, *Phys. Rev. B* **88**, 235409 (2013).
- ³⁷ T. Fujisawa and C. Lin, Plasmon modes of coupled quantum Hall edge channels in the presence of disorder-induced tunneling, *Phys. Rev. B* **103**, 165302 (2021).
- ³⁸ I. Safi, and H. J. Schulz, Transport in an inhomogeneous interacting one-dimensional system, *Phys. Rev. B* **52**, R17040(R) (1995).
- ³⁹ C. Altimiras, H. le Sueur, U. Gennser, A. Cavanna, D. Maily, and F. Pierre, Non-equilibrium edge-channel spectroscopy in the integer quantum Hall regime. *Nat. Phys.* **6**, 34 (2010).
- ⁴⁰ H. Frahm, C. von Zobeltitz, N. Maire and R. J. Haug, Fermi-edge singularities in transport through quantum dots, *Phys. Rev. B* **74**, 035329 (2006).
- ⁴¹ H. A. Fertig and B. I. Halperin, Transmission coefficient of an electron through a saddle-point potential in a magnetic field, *Phys Rev B* **36**, 7969 (1987).
- ⁴² T. Ihn, *Semiconductor Nanostructures: Quantum states and electronic transport*, Oxford Univ. Pr. (2009).
- ⁴³ H. Kamata, N. Kumada, M. Hashisaka, K. Muraki, and T. Fujisawa, Fractionalized wave packets from an artificial Tomonaga–Luttinger liquid. *Nat. Nanotech.* **9**, 177 (2014).
- ⁴⁴ C. J. Lin, M. Hashisaka, T. Akiho, K. Muraki, and T. Fujisawa, Quantized charge fractionalization at quantum Hall Y junctions in the disorder dominated regime, *Nature Commun.* **12**, 131 (2021).